Electrocatalytic Activity of Gold and Gold–Based Bimetallic Nanoparticles Derived from Their Surface Topography

Jin Wang, [a,b] Jing Wang,[d] Hong Li,[a] Weiliu Fan, [d] Dayang Wang*[c], and Haibing Xia*[a]

[a] State Key Laboratory of Crystal Materials, Shandong University, Jinan 250100, P. R. China
[b] Heze Branch, Qilu University of Technology (Shandong Academy of Sciences),
Heze 274000, P. R. China
[c] State Key Laboratory of Inorganic Synthesis and Preparative Chemistry,
College of Chemistry, Jilin University, Changchun 130012, P. R. China
[d] School of Chemistry and Chemical Engineering, Shandong University,
Jinan 250100, P. R. China
*Correspondence: hbxia@sdu.edu.cn; wangdayang@jlu.edu.cn

Table of Contents

Experimental Procedures

Materials. Hydrogen tetrachloroaurate(III) hydrate ($HAuCl_4$, 99.9%, metals basis, Au > 49%, min), sodium borohydride ($NaBH_4$, 99%), ethanol (C_2H_5OH), potassium hydroxide (KOH), ascorbic acid (AA, 99%), cetyltrimethylammonium chloride (CTAC, 99%) and trisodium citrate dehydrate ($Na_3C_6H_5O_7$, 99%) were purchased from Sinopharmacy Company (Shanghai, China). Sodium tetrachloropalladate (II) hydrate (Na_2PdCl_4, 99%), potassium hexachloropalladate (IV) (K_2PdCl_6, 99%), potassium hexachloroplatinate (IV) (K_2PtCl_6, 99%), sodium hexachloroiridate(III) hydrate ($Na_3IrCl_6 \cdot xH_2O$, 99%), silver nitrate ($AgNO_3$, 99%), cuprous chloride (CuCl, 99%), and commercial Pt/C catalysts were purchased from Alfa Aesar (Shanghai, China). The chemicals were used as received. The water in all experiments was prepared in a three stage Millipore (A10) purification system and has a resistivity of > 18 MΩ cm^{-1}. Prior to the synthesis of nanoscale Au particles, the aqueous solution of $HAuCl_4$ (1 wt%) was prepared and stored in the fridge (4 °C) to prevent its hydrolysis, which can be used within two weeks. The glassware and stir bars were thoroughly cleaned with aqua regia solutions consisted of HCl (37%) and HNO_3 (65%) with a volume ratio of 3:1, followed by thorough rinsing with H_2O. *Caution: Aqua Regia solutions are dangerous and must be used with extreme care and never stored the solutions in closed containers.*

Synthesis of Quasi-spherical 3 nm Au Particles (Au_3^{QS} particles) via $NaBH_4$ Reduction. 0.10 mL of an aqueous solution of $HAuCl_4$ (1 wt%) and 0.22 mL of an aqueous solution of citrate (1 wt%) were sequentially added into one vial containing 8 mL of H_2O under stirring at room temperature. Next, 0.15 mL of a freshly prepared ice-cold $NaBH_4$ solution (200 mM) was injected quickly into the citrate-$HAuCl_4$ solution under vigorous stirring. Then, the mixed solution was stirred for at least 3 h for the complete decomposition of excess $NaBH_4$.

Synthesis of Quasi-spherical 6 nm Au Particles (Au_6^{QS} particles) via Pre-Mixing Method. 6 nm Au particles was prepared according to our reported recipe with slight modifications.[1] 0.50 mL of an aqueous solution of $HAuCl_4$ (1 wt%) and 2.50 mL of an aqueous solution of citrate (1 wt%) were mixed under stirring at the room temperature. After the incubation of about 14 min, the resulting citrate-$HAuCl_4$ solution was quickly injected into 47.50 mL of boiling water under vigorous stirring. The reaction solution was further refluxed for 30 min under stirring to warrant formation of uniform quasi-spherical 6 nm Au particles.

Synthesis of Quasi-spherical 16 nm Au Particles (Au_{16}^{QS} particles) via Frens Method. 1.50 mL of an aqueous solutions of citrate (1 wt%) was added into 48.50 ml of boiling water containing the $HAuCl_4$ (1 wt%, 0.50 mL), followed by further refluxing of the reaction solution for 30 min to warrant formation of uniform quasi-spherical 16 nm Au particles. Note that the final concentration of $HAuCl_4$ in the reaction solution with a total volume of 50.00 mL was 0.01 wt%.

Synthesis of Quasi-Spherical 50 nm Au Particles (Au_{50}^{QS} particles) by Seeded Growth Method. 0.20 mL of an aqueous solution of citrate (1 wt%), 3.00 mL of seed solution (16 nm Au particles as seeds), and 0.50 mL of an aqueous solution of $HAuCl_4$ (1 wt%) were quickly injected into 46.30 mL of boiling water under vigorous stirring. The reaction solution was further refluxed for 30 min under stirring to warrant the formation of uniform quasi-spherical 50 nm Au particles. Note that an extra aqueous solution of citrate (1.30 mL, 1 wt%) was added into the reaction solution before the reaction started to cool to room temperature.

Synthesis of Au_{10-60}^{AG}. Au_{10-60}^{AG} was prepared according to our reported method.[2] 0.74 mL of 6 nm Au particles (1.76×10^{13} /mL) and 1.26 mL of 16 nm Au particles (1.15×10^{12} /mL) were added to one vial. The mixture of two-sized particles was stirred for 30 min at room temperature to ensure the formation of a homogeneous dispersion, followed by addition of an aqueous NaCl solution (0.50 mL, 400 mM) and slightly shaking for 1 min. After 12 h, the supernatant of the particles dispersion became transparent, leaving black precipitates at the bottom.

Synthesis of Au_3^{NW} @Pd(IV). The synthetic procedure is same to that for Au_3^{NW} @Pd except that the aqueous solutions of Na_2PdCl_4 was replaced by K_2PdCl_6 (0.13 mL, 5 mM).

Synthesis of Au_3^{NW} @Pt(IV). The synthetic procedure is same to that for Au_3^{NW} @Pd except that the aqueous solutions of Na_2PdCl_4 was replaced by K_2PtCl_6 (0.13 mL, 5 mM). And the Au-to-Pt precursors molar ratio is still 10.

Synthesis of Au_3^{QS} @Pd Particles. The synthetic procedure is same to that for Au_3^{NW} @Pd except that the aqueous solutions of Au_3^{NW} NPs was replaced by Au_3^{QS} NPs. And the Au-to-Pd precursors molar ratio is still 10.

Synthesis of Au_{10-60}^{AG}@Pd. The synthetic procedure is same to that for Au_3^{NW} -Pd except that the aqueous solutions of Au_3^{NW} NPs was replaced by Au_{10-60}^{AG} NPs. And the Au-to-Pd precursors molar ratio is still 10.

Synthesis of Au_{70}^{TOH} @Pd^{nL} NPs. The non-full coverage of Pd deposition prepared by ascorbic acid aims to achieve the controlled epitaxial growth of Pd atomic layers (denoted as nL) on the Au_{70}^{TOH} NP. Au_{70}^{TOH} @$Pd^{0.25L}$ were prepared by the overgrowth of Pd on the preformed Au_{70}^{TOH}. A typical procedure was as follows. The pH value of the aqueous CTAC solution containing Au_{70}^{TOH} (2.00 mL) was firstly adjusted to 3.3 with an aqueous HCl solution, followed by sequential addition of aqueous solutions of Na_2PdCl_4 (1 mM, 25.0 µL) and AA (2 mM, 25.0 µL). Note that the molar ratio of Pd precursor to Au_{70}^{TOH} was 1:160. The reaction mixture was incubated for 3 h at room temperature with stirring. Lastly, the resulting Au_{70}^{TOH} @$Pd^{0.25L}$ were collected and washed three times with Milli-Q water after the centrifugation (at 7000 rcf for 6 min) , followed by the redispersion into an aqueous solution containing citrate (2 mM) and KCl (4 mM) for further use.

Characterization. Transmission electron microscopy (TEM) and high-resolution TEM (HRTEM) images were obtained with a JEOL JEM-2100F transmission electron microscope operating at an acceleration voltage of 200 kV. Elemental mapping images were acquired by energy dispersive X-ray spectroscopy (EDS) using a JEOL JEM-2100F electron microscope equipped with a STEM unit.

Electrochemical Characterization. Cyclic voltammetric (CV) and linear sweep voltammetry (LSV) measurements were performed on a standard three-electrode electrochemical workstation (CHI 660D). A Pt wire and a Ag/AgCl (3 M KCl) electrode were selected as the counter electrode and reference electrode, respectively. Two different current collectors were employed as the working electrodes, i.e., glassy carbon electrode (GCEs) (3 mm in diameter) and a glassy-carbon rotating disk electrode (RDE) (area: ~0.196 cm^2).

The working electrodes for the measurements of electrode potentials of nanoscale Au particles were prepared by drop-coating the as-prepared nanoscale Au particles onto glassy carbon electrodes (GCEs) (3 mm in diameter).

The bare GCEs were successively polished with 0.30 and 0.05 μm alumina slurry, followed by thoroughly rinsing with pure water and drying at room temperature before use. In our work, to reduce the impact of ion concentrations on the electrode potentials of $PdCl_4^{2-}$/Pd couple and $AuCl_4^-$/Au couple, the concentration of Cl^- ions in the electrolytes were kept as 4 mM. Accordingly, the following electrode potentials were measured in the same conditions.

The LSV tests were scanned from 0.1 V to 0.9 V in N_2 –saturated 0.1 M $HClO_4$ solutions containing KCl, citrate or both at a scan rate of 0.01 V/s. Note that all of the samples have to be treated by the ligand exchange process before LSV tests. In addition, the prescanning is furtehr performed to remove the possible presence of the residual ligands on their surfaces. The optimal concentrations of citrate and Cl^- ions used for ligand exchange process of the as-prepared nanoscale Au particles were determined to be 2 mM and 4 mM, respectively. Both the purification procedure and ligand exchange process can guarantee the repeatability in the values of electrode potentials of samples during the tests because these samples possess the same ligands on their surfaces already. Note that Nafion cannot be used to fix the samples on the working electrode used for measurements of electrode potentia of samples. And all samples should be tested immediately after being loaded onto GCEs to avoid the impact of the slight Oswald ripening on their morphology. Moreover, the aggregation of the as-prepared nanoscale Au particles on GCES during the sample preparation is inevitable. However, the electrode potential of such particle aggregates would be close to that of bulk one and has no any effect on the unique properties of the isolated particles.

Taking Au^{TOH}_{70} as an example, the removal of the excess ligands (CTAC in this case) is as follows. The as-prepared Au^{TOH}_{70} were redispersed into water, followed by the centrifugation of 3 times with Milli-Q wate and anothe round of centrifugation with an aqueous KCl solution (4 mM). Then, the resulting Au^{TOH}_{70} were redispersed into the aqueous solution containing citrate (2 mM) and KCl (4 mM). Next, the resulting Au^{TOH}_{70} were drop-coated onto one GCE after the purification procedure and ligand exchange process.

The pre-scanning is also necessary before the test of electrode potentials, which can remove the residual CTAC remaning on their surfaces. Then, the GCE coated with Au^{TOH}_{70} was prescanned in 0.1 M $HClO_4$ solution containing KCl (4 mM) from 0 to -1.0 V versus Ag/AgCl at a scan rate of 0.01 V/s. Eventually, the electrode potential of Au^{TOH}_{70} was obtained, which is close to the true electrode potential.

A typical procedure for the preparation of the GCE modified by the as-prepared Au^{NW}_{3} is as follows. 6 μL of an aqueous dispersion of the as-prepared Au^{NW}_{3} was drop-coated onto a freshly prepared bare GCE, followed by drying in air. Note that the as-prepared Au^{NW}_{3} also have to be treated by redispersing them into the aqueous solution containing citrate (2 mM) and KCl (4 mM).

A series CV measurements of nanoscale Au-Pd or Au-Pt particles were prepared by drop-coating them on freshly prepared bare GCEs, followed by drying in air. Then, 10 μL of the ethanol solution containing Nafion (1 wt %) was cast onto the surface of the GCE coated with samples, followed by drying in air for further use.

a) The LSV tests of glassy carbon electrode (GCE) coated with samples as working electrodes for the measurments of theri electrode potentials were scanned from 0.1 V to 0.9 V (vs Ag/AgCl, 3 M KCl) in N_2 –saturated 0.1 M $HClO_4$ solutions containing 4 mM KCl at a scan rate of 0.01 V/s.

b) The LSV tests of glassy-carbon rotating disk electrode (RDE) coated with samples as working electrodes for the measurments of their oxygen reduction reaction (ORR) activity were scanned from -0.04 V to 1.16 V (vs RHE) in an O_2-saturated 0.1 M KOH aqueous solution at a scan rate of 10 mV s^{-1} and a rotation speed of 1600 rpm.

c) The CV tests of GCE coated with samples as working electrodes for the measurments of electrochemically active surface area (ECSA) were scanned from −1.00 and 0.60 V in N_2–saturated 0.3 M KOH solution with a scan rate of 50 mV s^{-1}.

For ethanol or methanol oxidation in alkaline media, CVs were recorded between −0.60 and 0.40 V in N_2-saturated 0.3 M KOH containing 0.5 M ethanol or 1.0 M methanol solution at a scan rate of 20 mV s^{-1}, respectively.

d) The CV tests of GCE coated with samples as working electrodes for the measurments of de-convolution were scanned from −0.3 to 1.5 V (vs Ag/AgCl, 3 M KCl) in N_2-saturated 0.5 M H_2SO_4 at a scan rate of 50 mV s^{-1}.

The de-convolution of the CV curves of the as-prepared Au particles was implemented to decompose the total electrochemically accessible NP surfaces into the components of individual low-index facets. The standard potentials (vs Ag/AgCl, 3 M KCl) of the {110}, {100}, and {111} planes of Au electrodes in the aqueous H_2SO_4 solution (0.5 M) are around 1.14, 1.2, and 1.4 V, respectively. The CV curves of the as-prepared Au particles in N_2-saturated H_2SO_4 (0.5 M) were measured from −0.3 to 1.5 V at a scan rate of 50 mV s^{-1}, which were employed to estimate the percentage of their surface facets by deconvolution analysis.

e) The CV tests of RDE coated with Au@Pd samples as working electrodes for the measurments of the ORR activity were scanned from -0.04 V to 1.16 V (vs RHE) in N_2 and O_2-saturated 0.1 M KOH aqueous solution at a scan rate of 50 mV s^{-1}.

The fabrication of RDE as working electrodes for ORR measurements of the as-prepared nanoscale Au particles is as follows. The as-prepared nanoscale Au particles (including Au^{QS}_{3}, Au^{TOH}_{70}, Au^{Ag}_{10-60} and Au^{NW}_{3}) were able to deposit on carbon support (Ketjen carbon) by the ultrasonification of 30 min in one mixture of water and ethanol (40 wt % of Au on carbon) containing carbon black, which were simplified as nanoscale Au particles/C catalysts. The uniform catalysts ink was prepared by mixing the resulting nanoscale Au particles/C catalysts with 9 μL of Nafion solution (5 wt %), 21 μL ethanol and 120 μL of water under sonication for 30 min. Then, 40 μL of catalysts ink was dropped onto the RDEs, followed by drying at room temperature. And the commercial Pt/C catalysts (20 wt.%) were also tested for comparison.

Their catalytic activity toward ORR was recorded in 0.1 M KOH with a rotation speed of 1600 rpm. Solution ohmic drop (i.e., iR drop) was compensated. During the measurements, the disk potential was swept at 10 mV s^{-1}, while the ring potential was potentio-stated at 1.23 V versus RHE where peroxide oxidation occurred under diffusion control. The electron transfer number (n) was determined by the following equation:

$$n = 4 * I_D/(I_D + I_R/N),$$

where I_D was the disk current, I^R was the ring current, and N was the collection efficiency of the ring electrode that was determined to be 0.37 of our electrode.

Results and Discussion

Fig. S1. TEM images (a to g) of Au_{50}^{QS} particles (a), Au_{16}^{QS} particles (b), Au_{6}^{QS} particles (c), Au_{3}^{QS} particles (d), Au_{70}^{TOH} particles (e), Au_{10-60}^{AG} (f), and Au_{3}^{NW} (g).

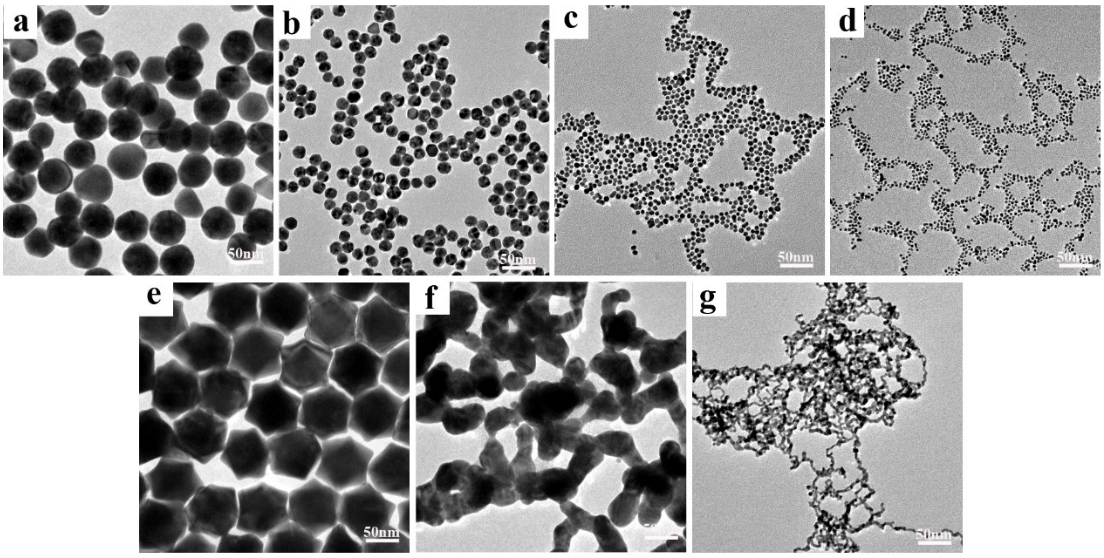

Fig. S2. (A) Normalized LSVs of GCE modified with Au^{NW}_3 treated with the mixed citrate-KCl solution, in which the concentration of Cl⁻ ions was varied from 0 (a, black curve) to 1 (b, red curve), 2 (c, blue curve), 3 (d, magenta curve), 4 (e, olive curve), and 5 mM (f, cyan curve) while that of citrate ions was remained as 2 mM. The LSV curves are recorded … V versu … ution co … e ions (2 mM). (B) Plots of the most negative electrode potential of the corresponding Au^{NW}_3 (in Fig. S2A). (C) Normalized LSVs of GCE modified with Au^{NW}_3 treated with the mixed citrate-KCl solution, in which the concentration of citrate ions was varied from 0 (a, black curve) to 1 (b, red curve), 2 (c, blue curve), 3 (d, magenta curve), 4 (e, olive curve), and 5 mM (f, cyan curve) while that of KCl was remained as 4 mM. … om 0.1 t … s Ag/AgCl at a scan rate of 0.01 V/s in 0.1 M $HClO_4$ solution containing KCl (4 mM). (D) Plots of the most negative electrode potential of the corresponding Au^{NW}_3 (in Fig. S2C).

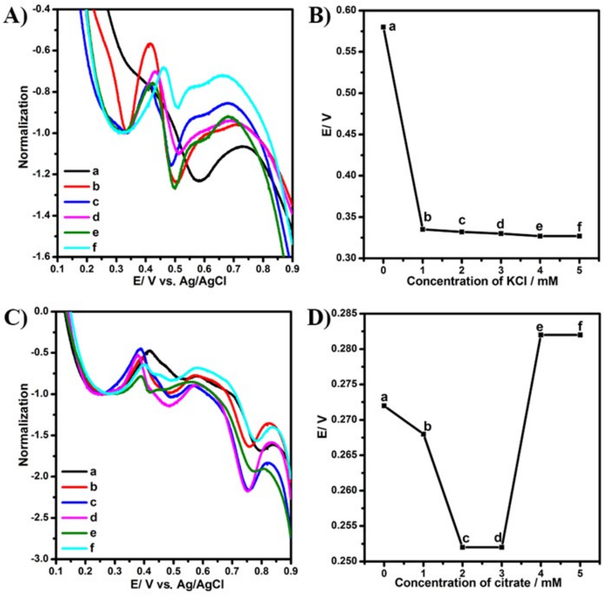

The ligands coated on the surface of NPs is of vital importance for their electrode potentials. [3–6] Thus, all of nanoscale Au particles have to be stabilized by the same ligands (citrate and Cl⁻ ions in this work) for better comparison by ligand exchange process. Moreover, to guarantee the stable negative shift in their electrode potential, the optimal concentrations of citrate and Cl⁻ ions for nanoscale Au particles were determined by after a series of electrochemical tests (Fig. S2 and S3). This is because the optimal concentrations of citrate and Cl⁻ ions render nanoscale Au particles as isolated as possible (citrate ions) and protecting them from oxidation (Cl⁻ ions). Accordingly, the optimal concentrations of citrate and Cl⁻ ions used for ligand exchange process of the nanoscale Au particles were determined by measuring their corresponding electrode potential after ligand exchange process. As expected, nanoscale Au particles after ligand exchange process at the optimal concentrations of citrate and Cl⁻ ions bear the most negative shift in their electrode potential. For instance, a series of Au^{NW}_3 were firstly treated with the mixed citrate-KCl solution, in which the concentration of KCl was varied from 0 to 1, 2, 3, 4, and 5 mM while that of citrate ions was remained as 2 mM. Then, the resulting Au^{NW}_3 were directly loaded onto GCE, and studied by LSV in 0.1 M $HClO_4$ solution containing citrate ions (2 mM) from 0.1 to 0.9 V versus Ag/AgCl at a scan rate of 0.01 V/s. (Fig. S2A and Table S1). Note that although in the presence of 0 M KCl, the oxidation of Au still can occur (Eq-1 and Eq-2). However, the electrode potential is rather high (Fig. S2), compared with those in the presence of KCl (1 ~ 5 mM). This is because nanoscale Au particles used in this work were prepared by reduction of $HAuCl_4$. Accordingly, the adsorption of some Cl⁻ ions on their surfaces is evitable, which has been studied previously. Consequently, Au atoms on the surfaces of nanoscale Au particles still can be oxidized.

$$Au + 4Cl^- = AuCl_4^- + 3e^- \ (0.792\ V\ vs\ Ag/AgCl) \qquad (Eq\text{-}1)$$

$$Au + 2Cl^- = AuCl_2^- + e^- \ (0.94\ V\ vs\ Ag/AgCl) \qquad (Eq\text{-}2)$$

Au^{NW}_3 treated with citrate ions alone show a large oxidation peak near at 580 mV in the LSV curve (Fig. S2A-a and Fig. S2B-a). However, the electrode potential of Au^{NW}_3 treated with the mixed citrate (2mM)-KCl solution (1 mM) dramatically decreases to 335 mV (Fig. S2A-b and Fig. S2B-b). With the increasing concentration of KCl solution (from 1 to 5 mM), the electrode potential of 3 nm Au NWs treated with the mixed citrate (2 mM)-KCl solution (1 to 4 mM) gradually decreases from 335 to 327 mV. When the concentration of KCl solution is bigger than 4 mM, their electrode potential is kept as 327 mV (Fig. S2A and Fig. S2B). Thus, the results indicate that the presence of Cl⁻ ions leads to the dramatic negative shift in electrode potential of Au^{NW}_3. In addition, the halide-dependent electrode potentials of Au^{NW}_3 also strongly suggest that the formation of these peaks are due to halide-assisted Au oxidation, which is consistent with the formation of Au metal oxidation in the presence of halides (Table S2).[7,8] As the high concentration of Cl⁻ ions can result in the aggregation of nanoscale Au particles, the concentration of Cl⁻ ions in this work is selected as 4 mM.

When the optimal concentration of KCl was determined, the impact of citrate ions on the electrode potential of Au^{NW}_3 were further investigated. Accordingly, a series of Au^{NW}_3 were also treated with the mixed citrate-KCl solution, in which the concentration of citrate ions was varied from 0 to 1, 2, 3, 4, and 5 mM while that of KCl was remained as 4 mM. Then, the resulting Au^{NW}_3 were directly loaded onto GCE, and studied by LSV in 0.1 M $HClO_4$ solution containing KCl (4 mM) from 0.1 to 0.9 V versus Ag/AgCl at a scan rate of 0.01 V/s (Fig. S2C and Table S1). One can clearly see that the presence of Cl⁻ ions in advance on the surface of Au^{NW}_3 can render them bear a more negative electrode potential (272 mV, Fig. S2B-a). However, with the increasing concentration of citrate ions, their electrode potential firstly decreases and then increased (Fig. S2C and D).

Fig. S3. (A) LSVs of GCEs modified with Au_3^{NW} treated with the mixed citrate-KCl solution, which were measured in 0.1 M $HClO_4$ solution containing KCl (4 mM) from 0.1 to 0.9 V versus Ag/AgCl at a scan rate of 0.01 V/s. The concentration of citrate ions in the mixed citrate-KCl solution was varied from 0 (a1 and b1) to 1 (a2 and b2), 2 (a3 and b3), 3 (a4 [illegible] M. In each patch, f[illegible] were test[illegible] Au_3^{NW} [illegible]es of the electrode potential obtained. (B) Plots of the values of the electrode potential peaks (i, ii, and iii) of the corresponding Au_3^{NW} in Fig. S3A, as shown by the black arrows.

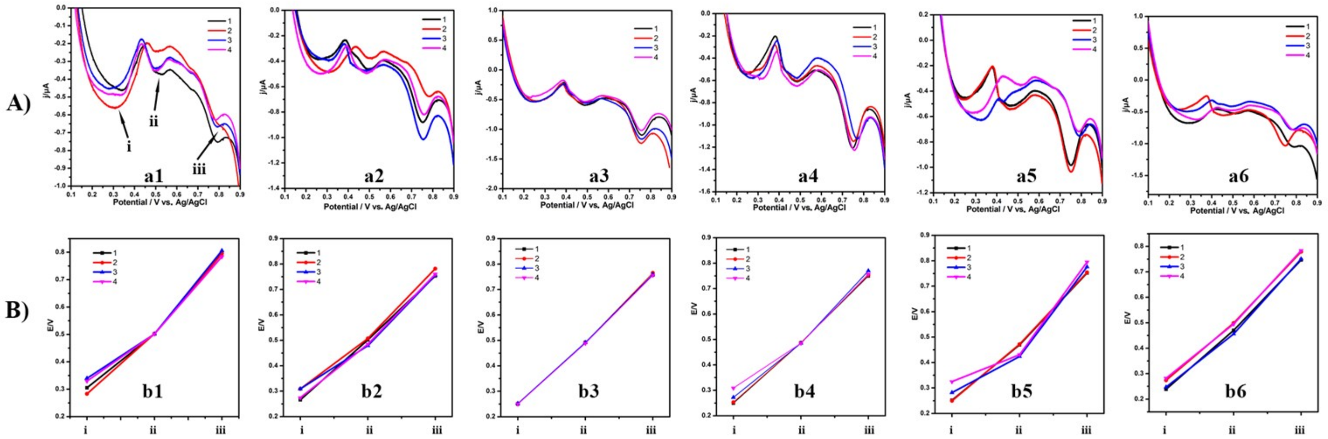

On the basis of the results multiple tests of different batches of Au_3^{NW} (Fig. S3 and Table S3), it is found that when the concentration of citrate ions is lower than 2 mM, the electrode potential of Au_3^{NW} are rather higher. This is possibly because Au_3^{NW} particles on the surfaces of GCEs is rather easily aggregated due to their length. And the sintering during the testing would lead to the decrease of active sites and further leading to the increase in their electrode potential. While the citrate ions is higher than 2 mM, the citrate ions will replace the Cl⁻ ions[3,6] on the surfaces of 3 nm NWs, thus also leading to the increase in their electrode potential.

It is known that citrate ions are one type of weak stabilizers for Au NPs, compared with thiols, amines and Cl⁻ ions. And a proper amount of citrate ions[9] just slightly reduces the chance for the sintering of Au_3^{NW} particles and their main role in the electrode potentials of Au_3^{NW} particles is not to impact the adsorption of Cl⁻ ions on the surfaces of Au_3^{NW} particles. However, high concentration of citrate still can impact the adsorption of Cl⁻ ions on the surface of Au particle due to the occupation of citrate ions [6,10]. Consequently, the role of a proper concentration of citrate ions for other Au particles in this work is to reduce the chance of the aggregation and sintering, and guarantee the adsorption of Cl⁻ ions on their surfaces.

Fig. S4. LSVs of the bare GCE (without any Au particles) measured in 0.1 M $HClO_4$ solution in the absence (a, black plot) and presence of citrate (2 mM) (b, red plot) or KCl (4 mM) (c, blue plot), from 0.1 to 0.9 V versus Ag/AgCl at a scan rate of 0.01 V/s.

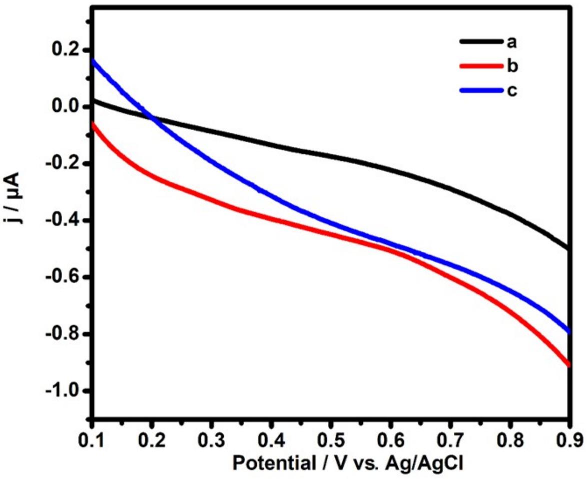

The LSV tests of the bare GCE (without any Au particles) measured in 0.1 M $HClO_4$ solution containing citrate ions (or KCl) indicate that the oxidation peaks in the LSV curves of GCEs coated with Au particles are not related with the bare GCEs, the citrate and Cl^- ions. In view of stability and negative shift in the electrode potential of Au_{3}^{NW}, the optimal concentrations of citrate ions and Cl^- ions are selected as 2 mM and 4 mM, respectively, which also applied to other types of nanoscale Au particles. Note that the presence of background currents is attributed to the presence of these agents (such as $HClO_4$, citrate and KCl) in the electrolyte solutions.

Fig. S5 of GCE modified with Au^{TOH}_{70} particles treated without (black plot) and with (red plot) the mixed solution co mM) and (2 mM). The were me us Ag/AgCl at a scan rate of 0.01 V/s. TEM images of Au^{TOH}_{70} (b) Au^{QS}_{6} (c), and Au^{NW}_{3} (d) after their loading process on GCEs, which were transferred to copper grids.

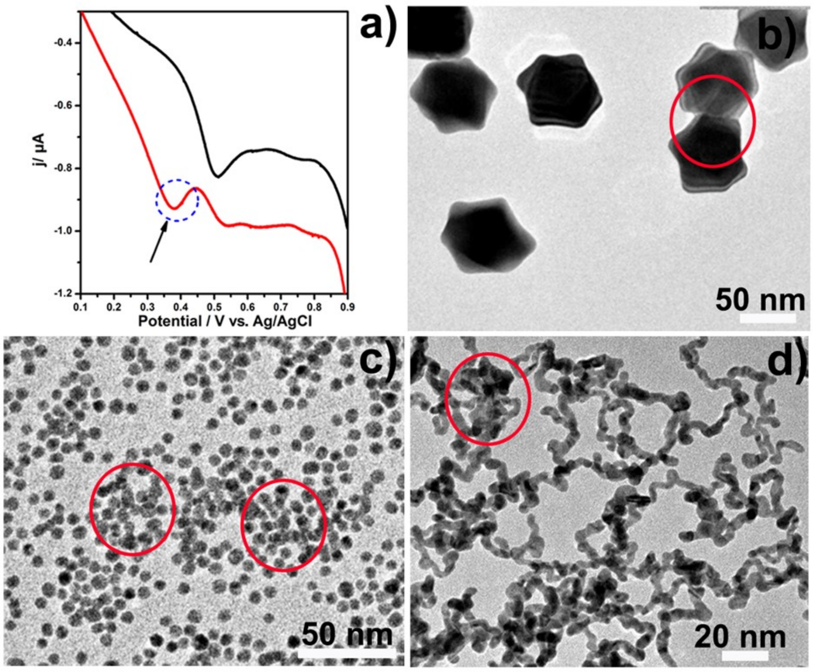

Au^{TOH}_{70} particles were synthesized by using CTAC ligands. The CTAC ligands strongly absorbs on the surfaces of Au^{TOH}_{70} particles to stabilize their active facets. Thus, the CTAC ligands on Au^{TOH}_{70} particles have to be removed before the tests via the ligand exchange process with the mixed solution containing citrate (4 mM) and KCl (2 mM). If Au^{TOH}_{70} particles are mainly dispersed on the surfaces of GCEs (not particle aggregates), the change in electrode potential should appear in the range of 0.7 ~ 0.8 V between their LSV tests under different conditions. However, the more negative electrode potential peak (indicated by the black arrow) appears in the range of 0.35 ~ 0.5 V (Fig. S5a), indicating the exposure of active sites of Au^{TOH}_{70} particles after the ligand exchange process and Au^{TOH}_{70} particles are mainly dispersed on the surfaces of GCEs.

As shown in Fig. S5b-c, most of Au^{TOH}_{70} and Au^{QS}_{6} are well dispersed, accompanied with some particle aggregates (enclosed by red circle) led by the sintering during the loading process on GCEs (or transferring process from GCEs to copper grids). As for Au^{NW}_{3} (Fig. S5d), there is hardly any change their morphology except the connecting parts (enclosed by red circle) become larger due to the sintering. Accordingly, the ligand exchange process for CTAC-coated Au^{TOH}_{70} with the mixed solution containing citrate (4 mM) and KCl (2 mM) is necessary.

Au^{QS} Au^{QS} Au^{QS} Au^{QS} Au^{TOH}

odified with , black p

particles (e, olive plot), Au^{AG}_{10-60} (f, navy plot), and Au^{NW}_{3} (g, violet plot), in which the electrode potential (in the range of 0.7 – 0.8 V) of such aggregates of nanoscale Au particles are highlighted by vertical lines, measured in $HClO_4$ solution (0.1 M) containing KCl (4 mM) from 0.1 to 0.9 V versus Ag/AgCl at a scan rate of 0.01 V/s.

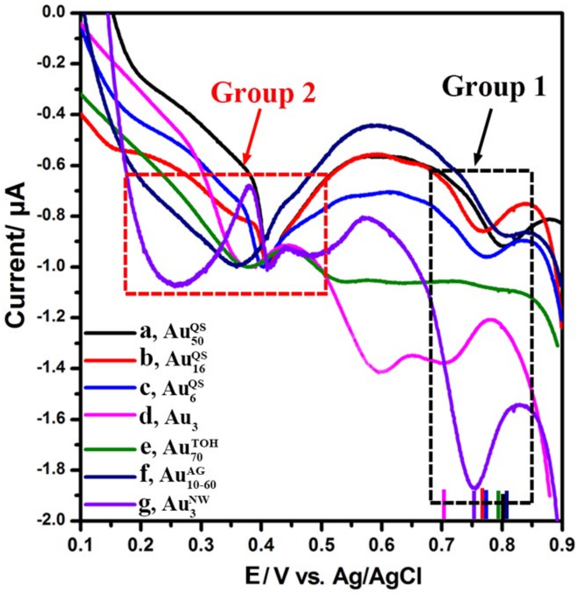

Group 1 is the values of their electrode potentials within the range of about 0.7 ~ 0.8 V and Group 2 is those within the range of about 0.25 ~ 0.5 V. The electrode potential in the range of 0.7 – 0.8 V corresonds to -the following electrochemical reaction: $Au + 4Cl^- = AuCl_4^- + 3e^-$ (0.792 V vs Ag/AgCl).

Fig. S7. A) LSV curve of bulk Au was scanned from 0.1 to 0.9 V versus Ag/AgCl at a scan rate of 10 mV s^{-1} in 0.1 M $HClO_4$ solution containing 4 mM KCl. B) CV curve of bulk Au was scanned from 0.1 to 1.0 V versus Ag/AgCl at a scan rate of 50 mV s^{-1} in 0.1 M $HClO_4$ solution containing 4 mM KCl. The inset shows the optical image of bulk Au.

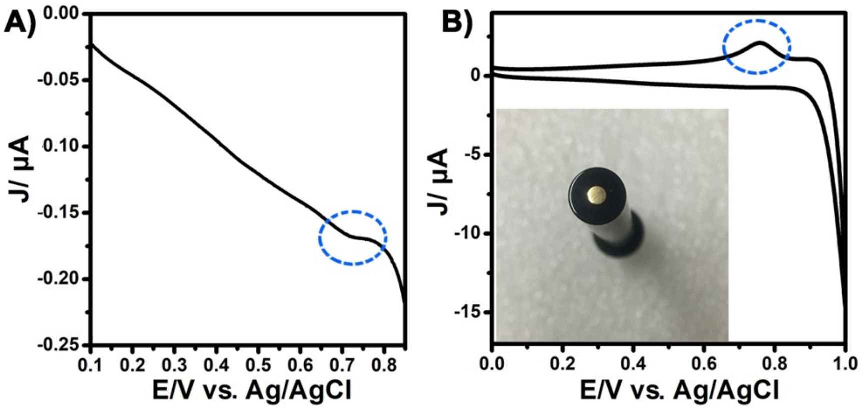

The LSV and CVs of bilk gold electrodes were investigated under the similar experimental conditions and shown in Fig. S7. It can be seen that the electrode potentials of bulk gold in both LSV and CV curves are about 0.76V versus Ag/AgCl, which is close to the standard electrode potential of bulk gold.

Fig. S8. LSV curves of GCEs modified with Au_3^{QS} NPs recorded at the first scan (black plot) and the fifth scan (red plot). The LSV curves were measured in 0.1 M $HClO_4$ solution containing KCl (4 mM) from 0.1 to 0.9 V versus Ag/AgCl with a scan rate of 0.01 V/s.

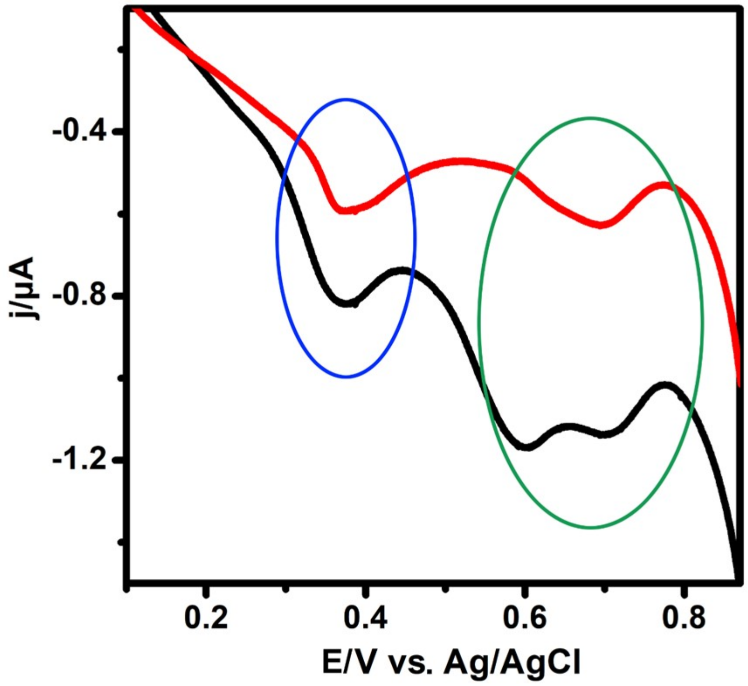

To demonstrate whether the variation in the electrode potential of aggregates of nanoscale Au particles has an effect on the that of isolated nanoscale Au particles, LSV of GCEs modified with Au_3^{QS} NPs recorded at the first cycle was compared with that recorded at the fifth cycle (Fig. S8). It is found that there is hardly any chang in the electrode potential of isolated nanoscale Au particles in the LSV curve of Au_3^{QS} NPs (blue circle) while that of aggregates of nanoscale Au particles indeed changes (green circle) due to the sintering between Au NPs during the scanning. The result indicates that the variation in the electrode potential of aggregates of nanoscale Au particles has hardly an effect on the that of isolated nanoscale Au particles.

Fig. S9. TEM images (a, c, e and g) of Au^{TOH}_{70}@Pd particles (a), Au^{QS}_{3}@Pd particles (c), Au^{AG}_{10-60}@Pd (e), and Au^{NW}_{3}@Pd NWs (g); HAADF-STEM-EDS images and the overlapping images of single Au^{TOH}_{70}@Pd particle (b), Au^{QS}_{3}@Pd particle (d), NW of Au^{AG}_{10-60}@Pd (f), and Au^{NW}_{3}@Pd (h). The Au-to-Pd precursors molar ratio in all the simples is 10.

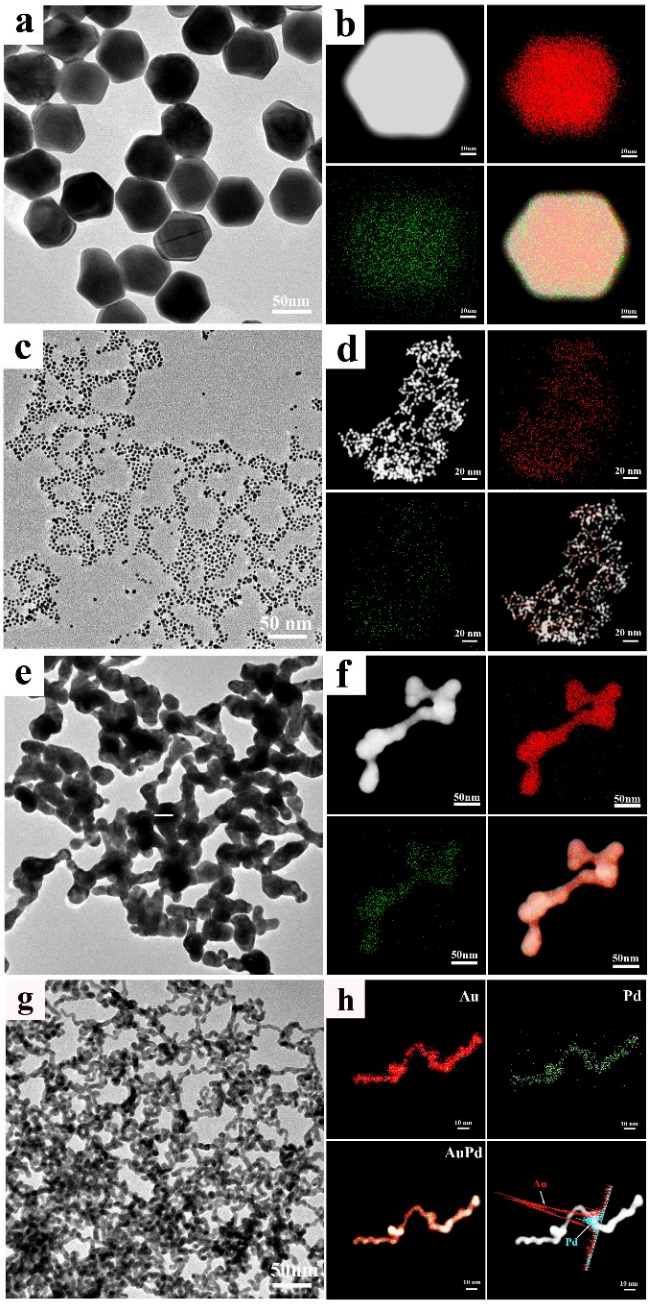

On the basis of the EDS results, the resulting nanoscale Au@Pd particles were indeed composed of elemental Au and Pd; the contents of Pd are increased from 0.89% ± 0.05% for Au^{TOH}_{70}-Pd particles to 1.56% ± 0.09% for Au^{QS}_{3}-Pd particles, 2.5% ± 0.13% for Au^{AG}_{10-60}-Pd and 8.0% ± 0.35%for Au^{NW}_{3}-Pd, respectively. The difference in the values between bulk percentage and surface coverage is due to the fact that the ECSA value (149.2 m^2 g^{-1}) of Au^{NW}_{3} particles is about 1.67 times larger than that (89.6 m^2 g^{-1}) of Au^{AG}_{10-60} particles, which can be calculated according to the CV curves in Fig. 5A.

Fig. S10 (A) High resolution TEM image of the surface of one Au_{10-60}^{AG} (B) CV curve of Au_{10-60}^{AG} obtained in 0.5 H_2SO_4 (black curves), which is fitted by combination of the components of {111} facets (green curve), {110} facets (purple curve) and {100} facets (blue curve) present on the NP surfaces. To reduce the errors in the fractions of {111}, {100}, and {110} facet of Au particles, five curves of Au_{10-60}^{AG} particles were used to obtain the average fractions of {111}, {100}, and {110} facet by deconvolution of the corresponding CV curves. And the curve which is rather close to the average value was selected. (C-D) Histogram of the values of $R_{(hkl)}^{Au}$ (C) of the surfaces of Au_{10-60}^{AG} NPs derived from the de-convolution of their CV cures and the values of the production of $f_{AGR\{hkl\}}^{Au/Pd}$(shaded by dark gray in C) and $\epsilon_{ST\{hkl\}}^{Au/Pd}$ obtained for AGR with $PdCl_4^{2-}$ ions, calculated according to Equations (5) and (6), respectively.

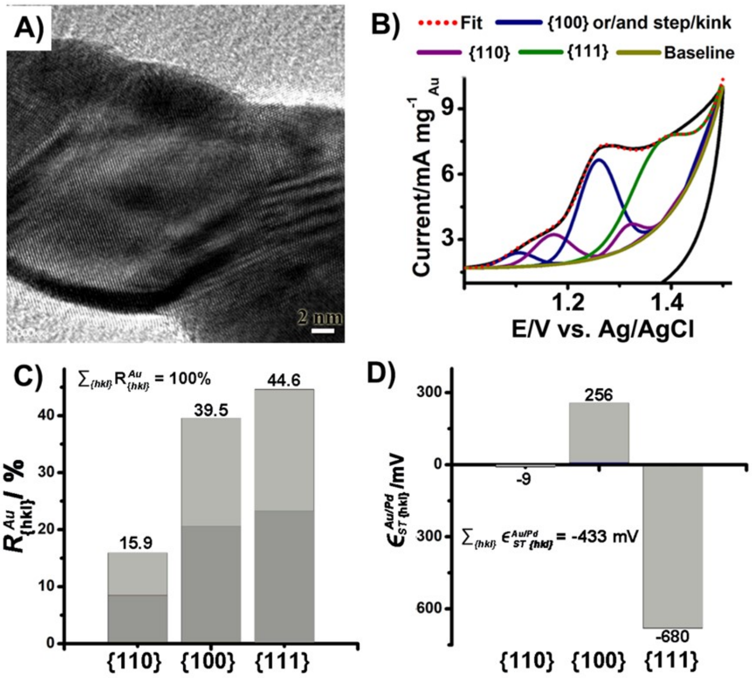

Fig. S11 (A) High resolution TEM image of the surface of one Au_3^{NW} (B) CV curve of Au_3^{NW} obtained in 0.5 H_2SO_4 (black curves), which is fitted by combination of the components of {111} facets (green curve), {110} facets (purple curve) and {100} facets (blue curve) present on the NP surfaces. To reduce the errors in the fractions of {111}, {100}, and {110} facet of Au particles, five curves of Au_3^{NW} particles were used to obtain the average fractions of {111}, {100}, and {110} facet by deconvolution of the corresponding CV curves. And the curve which is rather close to the average value was selected. (C-D) Histogram of the values of $R_{(hkl)}^{Au}$ (C) of the surfaces of Au_3^{NW} NPs derived from the de-convolution of their CV cures and the values of the production of $f_{AGR\{hkl\}}^{Au/Pd}$(shaded by dark gray in C) and $\epsilon_{ST\{hkl\}}^{Au/Pd}$ obtained for AGR with $PdCl_4^{2-}$ ions, calculated according to Equations (5) and (6), respectively.

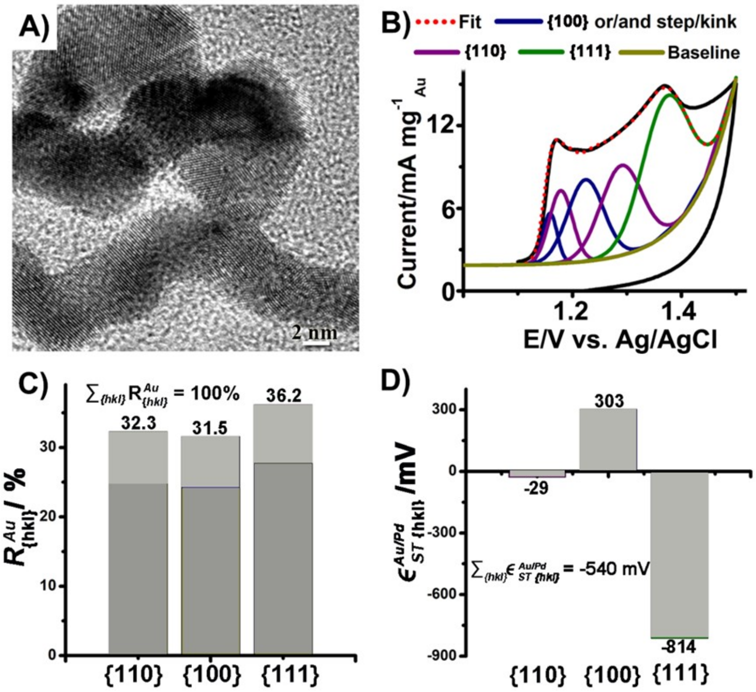

Fig. S12 (A) High resolution TEM image of the surface of one Au_3^{QS} (B) CV curve Au_3^{QS} obtained in 0.5 H_2SO_4 (black curves), which is fitted by combination of the components of {111} facets (green curve), {110} facets (purple curve) and {100} facets (blue curve) present on the NP surfaces. To reduce the errors in the fractions of {111}, {100}, and {110} facet of Au particles, five curves of Au_3^{QS} particles were used to obtain the average fractions of {111}, {100}, and {110} facet by deconvolution of the corresponding CV curves. And the curve which is rather close to the average value was selected. (C-D) Histogram of the values of $R_{\{hkl\}}^{Au}$ (C) of the surfaces of Au_3^{QS} NPs derived from the de-convolution of their CV cures and the values of the production of $f_{AGR\{hkl\}}^{Au/Pd}$(shaded by dark gray in C) and $\epsilon_{ST(hkl)}^{Au/Pd}$ obtained for AGR with $PdCl_4^{2-}$ ions, calculated according to Equations (5) and (6), respectively.

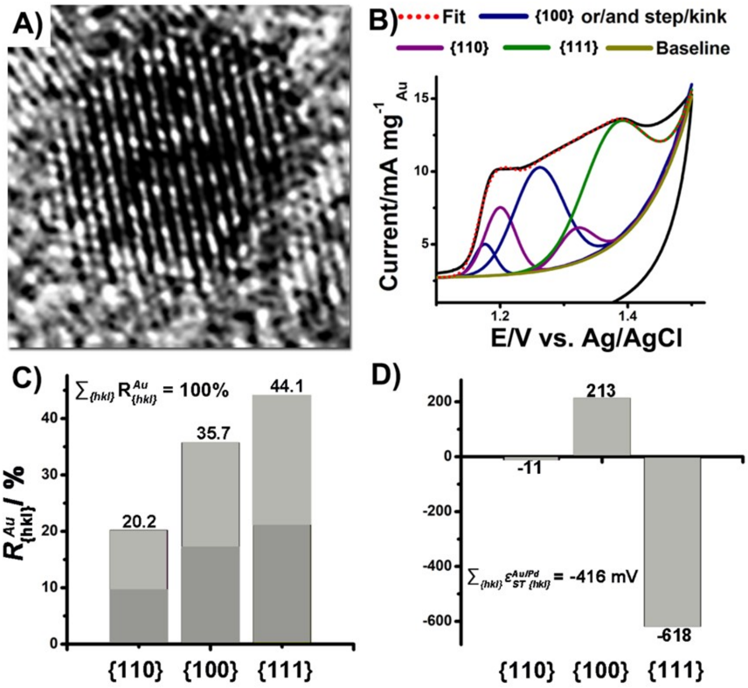

Fig. S13. CV curves of GCEs modified by Au^{TOH}_{70} particles with different Pd deposition: Au^{TOH}_{70} particles (a, black curve), Au^{TOH}_{70} @Pd$^{0.25\ L}$ particles (b, blue curve), and c) Au^{TOH}_{70} @Pd$^{0.35\ L}$ (c, green curve), measured in 0.5 M H_2SO_4 aqueous solution with a scan rate of 50 mV s^{-1}.

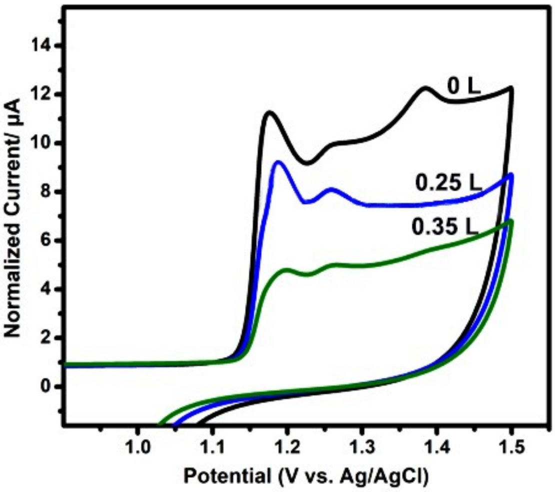

The deposition of Pd on nanoscale Au particles shown in this work is the initial and final state. Therefore, the difference in deposition of Pd on different facets of Au particles cannot be observed. Thanks to without the use of any reducing agent, deposition of Pd on different facets of nanoscale Au particles on which AGR can occur can investigated in detail. Since Au^{TOH}_{70} particles have the well-defined {111} and {110} facets, the deposition of Pd on Au^{TOH}_{70} particles as a typical sample were investigated in detail to show the difference in Pd position on their facets (Fig. S13). In the anodic CV scans of metallic Au in acidic solution, the peak positions in the region of 1.10–1.50 V (a, black curve) can be attributed to the formation of a monolayer of gold oxide [11,12]. The oxidation peaks of {111} facets of Au^{TOH}_{70} particles are located at around 1.37 V, while those of {110} facets are at around 1.20 and 1.28 V (black curve in Fig. S13). However, the oxidation peak located at around 1.37 V disappears (b, blue curve) in the CV curve of Au^{TOH}_{70} particles with a non-full Pd coverage (named as Au^{TOH}_{70} @Pd$^{0.25\ L}$ particles because the current Pd amount is about 0.25 of the amount for a monolayer of Pd full coverage on the basis of the calculation). This indicates that Pd atoms are firstly deposited on the {111} facets of Au^{TOH}_{70} particles when the number of Pd layers is below 1 layer. When the Pd amount was further increased (the Pd amount is equal to 0.35 of the amount for a monolayer of Pd full coverage, Au^{TOH}_{70} @Pd$^{0.35\ L}$ particles), the relative intensity of the oxidation peak in the CV of Au^{TOH}_{70} @Pd$^{0.35\ L}$ particles located at around 1.20 V decreased (c, green curve), indicating that the Pd atoms begin to cover the {110} facets of the surfaces of Au^{TOH}_{70} particles. These results indicate that the electrode potential of {111} facets on Au^{TOH}_{70} particles is lower than that of {110} facets.

Fig. S14. LSV curves of Au_{3}^{QS}/C (a), Au_{70}^{TOH}/C (b), Au_{10-60}^{AG}/C (c), and Au_{3}^{NW}/C (d).

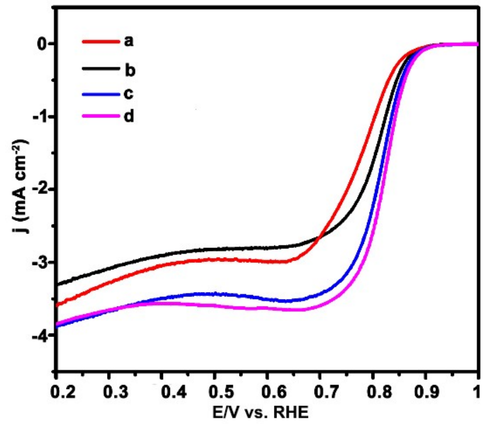

To further demonstrate their surface topography-induced reducing activity and their technical applicability, the as-prepared Au_{70}^{TOH}, Au_{3}^{QS}, Au_{10-60}^{AG}, and Au_{3}^{NW} NPs were harnessed as electro-catalysts for oxygen reduction reaction (ORR). Fig. S14 shows the LSV curves of Au_{3}^{QS}/C (a), Au_{70}^{TOH}/C (b), Au_{10-60}^{AG}/C (c), and Au_{3}^{NW}/C (d) in an O_2-saturated 0.1 M KOH aqueous solution at a scan rate of 10 mV s^{-1} and a rotation speed of 1600 rpm. The onset potentials of Au_{3}^{NW}/C (0.971 V) are positive than that of Au_{3}^{QS}/C (0.951 V), Au_{70}^{TOH}/C (0.949 V), or Au_{10-60}^{AG}/C (0.955 V). Moreover, the half potential ($E_{1/2}$) of Au_{3}^{NW}/C (0.822 V) also exhibited a positive shift of 22 mV, 32 mV, and 12 mV than Au_{3}^{QS}/C (0.80 V), Au_{70}^{TOH}/C (0.79 V), or Au_{10-60}^{AG}/C (0.81 V), respectively. Furthermore, the diffusion-limited current density of Au_{3}^{NW}/C is 3.61 mA cm^{-2} at 1600 rpm (at 0.45 V), which is also much higher than that of the Au_{3}^{QS}/C (2.85 mA cm^{-2}), Au_{70}^{TOH}/C (2.98 mA cm^{-2}), and Au_{10-60}^{AG}/C (3.4 mA cm^{-2}). The coincidence between the electrocatalytic performance of Au NPs towards ORR and their potentials dictated by defects present on their (111) facets provides additional evidence to endorse the hypothesis

Fig. S15. Methanol-crossover effects test of commercial Pt/C catalysts (a) and Au_3^{NW} NPs (b), which were carried out at 0.7 V (*vs.* RHE) in a O_2-saturated 0.1 M KOH solution with a scan rate of 5 mV s^{-1} and with a rotation speed of 1600 rpm.

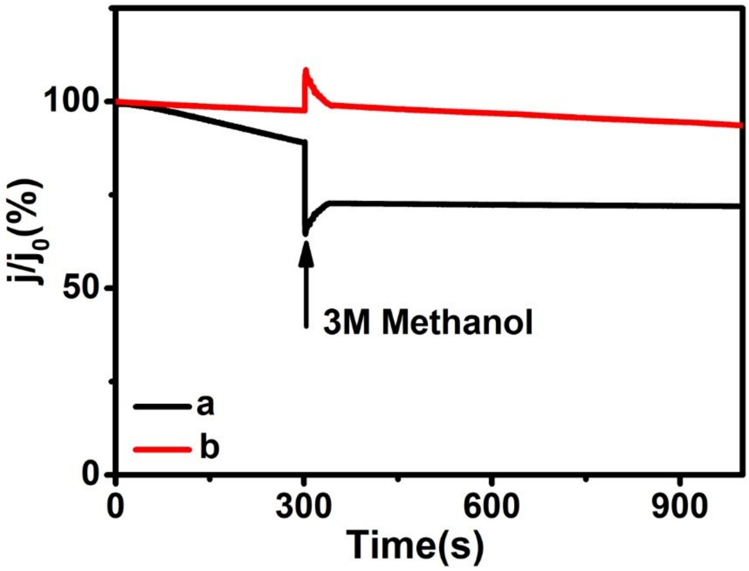

The resulting Au_3^{NW} NPs show a slight change in the relative currents while the commercial Pt/C catalysts (20 wt.%) show a significant drop in the relative currents and cannot be recovered.

Fig. S16. (A) TEM image (a) and HDAAF-STEM-EDS images (b) of the resulting Au_3^{NW}@Pd (IV) NWs, CV curves of GCEs modified by the resulting Au_3^{NW}@Pd (IV) NWs measured in 0.3 M KOH solution in the absence (c) and presence (d) of 0.5 M ethanol solution. (B) TEM image (e) and HDAAF-STEM-EDS images (f) of the resulting Au_3^{NW}@Pt (IV) NWs, CV curves of GCEs modified by the resulting Au_3^{NW}@Pt (IV) NWs measured in 0.3 M KOH solution in the absence (c) and presence (d) of 1.0 M methanol solution. The Au-to-Pd and Au-to-Pt precursors molar ratio both are 10.

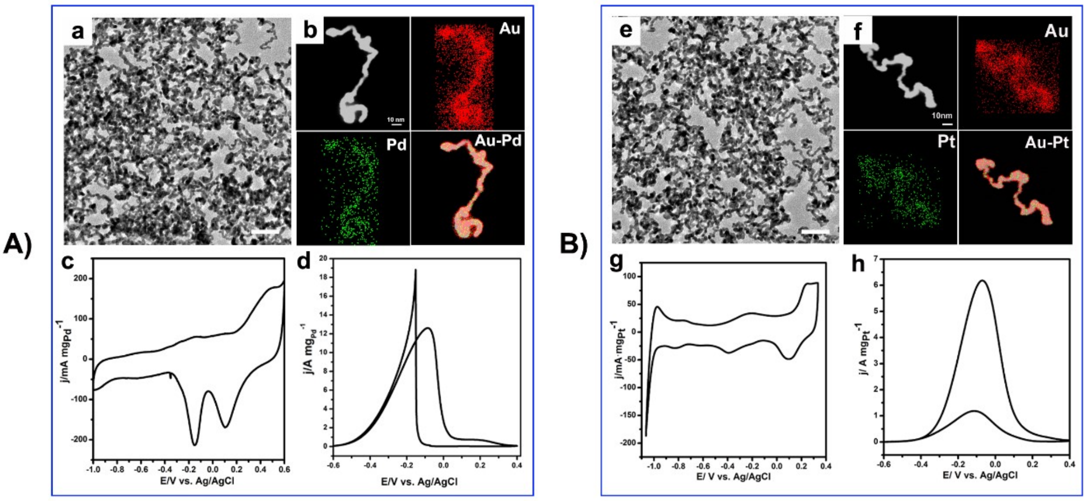

On the basis of the EDS results, the atomic fractions of Au and Pd in the as-prepared Au_3^{NW}@Pd (IV) NWs are about 94.5% and 5.5 %, respectively. In addition, the atomic fractions of Au and Pt in the as-prepared Au_3^{NW}@Pt (IV) NWs are about 94.0% and 5.0 %, respectively.

Fig. S17. CV curves (a), TEM images (b) and HDAAF-STEM-EDS images (c and d) of Au_3^{NW} @Cu (I) (A), Au_3^{NW} @Ag (B) and Au_3^{NW} @Ir (C).

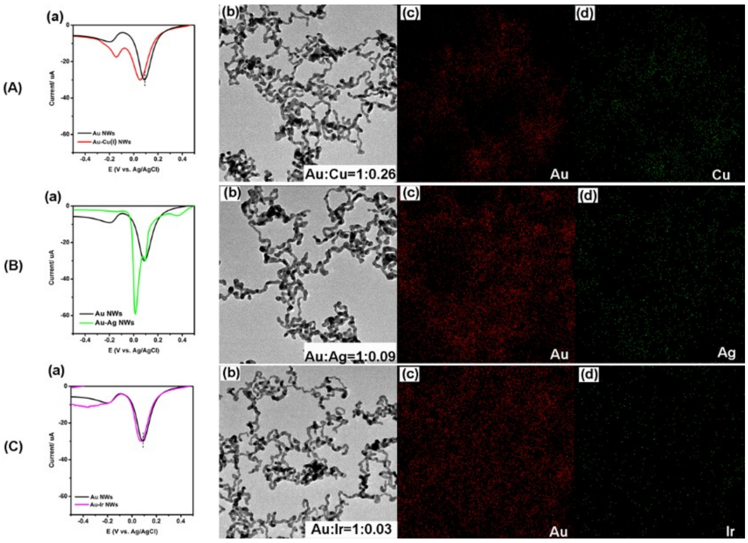

Similarly, Au_3^{NW} @Cu (I), Au_3^{NW} @Ir and Au_3^{NW} @Ag were prepared by AGR reaction of Au_3^{NW} particles with the corresponding metal ions (Cu^+ ion, Ir^{3+} ion and Ag^+ ions). Their CVs were recorded between −1.00 and 0.60 V in N_2–saturated 0.3 M KOH solution with a scan rate of 50 mV s^{-1}. There are no obvious reduction peaks of Cu and Ir in the CV curves of "Au_3^{NW} @Cu (I)" and "Au_3^{NW} @Ir". However, the potential of Au reduction peaks in their CVs were negatively shifted, indicating the formation of Cu and Ir. In addition, one obvious Ag reduction peak was observed in the CV curve of Au_3^{NW} @Ag.

Fig. S18. CV curves of RDE coated with Au^{NW}_{3}@$Pd_{20.7}$ NPs in N_2 saturated 0.1 M KOH aqueous solution at a scan rate of 50 mV s^{-1}.

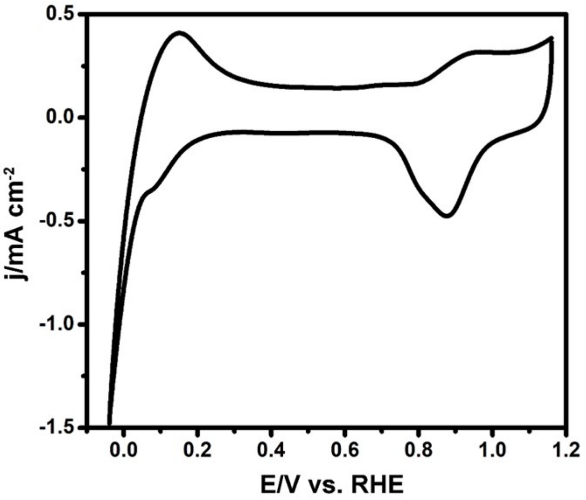

Table S1. Summarized values of the most negative electrode potentials of Au_3^{NW}, which were treated with different concentrations of Cl^- ions and citrate ions.

Concentrations of Cl^- or citrate ion	**a (0 mM)**	**b (1 mM)**	**c (2 mM)**	**d (3 mM)**	**e (4 mM)**	**f (5 mM)**
$E_{fixed\ [Citrate]}$/ V	0.580	0.335	0.332	0.330	0.327	0.327
$E_{fixed\ [Cl^-]}$/ V	0.272	0.268	0.252	0.252	0.282	0.282

Table S2. Summary of the electrode potential values of half-reactions.

Electrode Reaction	**E°/V vs NHE**	**E°/V vs Ag/AgCl(3M)**
$Cu^{+} + e^{-} = Cu$	0.521	0.311
$PdCl_4^{2-} + 2e^{-} = Pd + 4Cl^{-}$	0.591	0.381
$PdCl_6^{2-} + 2e^{-} = PdCl_4^{2-} + 2Cl^{-}$	1.29	1.08
$PtCl_6^{2-} + 2e^{-} = Pt + 6Cl^{-}$	0.726	0.516
$Ag^{+} + e^{-} = Ag$	0.7996	0.5896
$Ir^{3+} + 3e^{-} = Ir$	1.156	0.946
$AuCl_4^{-} + 3e^{-} = Au + 4Cl^{-}$	1.002	0.792
$AuCl_2^{-} + e^{-} = Au + 2Cl^{-}$	1.15	0.94
$Au^{3+} + 3e^{-} = Au$	1.498	1.288
$Au^{+} + e^{-} = Au$	1.692	1.482

Table S3. Summarized values of the electrode potential (peak i, ii, and iii) of samples shown in Fig. S3.

	Peak i/ V	Peak ii/ V	Peak iii/ V
a1 and b1	0.339	0.530	0.795
	0.305	0.502	0.790
	0.283	0.503	0.795
	0.330	0.502	0.784
a2 and b2	0.266	0.502	0.753
	0.309	0.507	0.782
	0.309	0.479	0.756
	0.274	0.485	0.760
a3 and b3	0.250	0.492	0.757
	0.252	0.491	0.765
	0.252	0.492	0.759
	0.250	0.489	0.756
a4 and b4	0.250	0.487	0.750
	0.253	0.487	0.753
	0.272	0.485	0.770
	0.309	0.485	0.757
a5 and b5	0.280	0.470	0.762
	0.282	0.424	0.776
	0.325	0.431	0.795
	0.286	0.514	0.788
a6 and b6	0.289	0.514	0.794
	0.267	0.456	0.761
	0.282	0.495	0.784
	0.309	0.491	0.794

Table S4. Summarized values of the most negative electrode potentials of Au^{QS}_{50}, Au^{QS}_{16}, Au^{QS}_{6}, Au^{QS}_{3} particle, Au^{TOH}_{70} particles, Au^{AG}_{10-60} and Au^{NW}_{3}.

Samples	**Fig. 1a**	**Fig. 1-b**	**Fig. 1-c**	**Fig. 1d**	**Fig. 1e**	**Fig. 1f**	**Fig. 1g**
Shape	quasi-spherical	quasi-spherical	quasi-spherical	quasi-spherical	TOH	aerogels	NWs
Surface construction	Wulff	Wulff	Wulff	Wulff	Defects	Defects	Defects
Average dimension	50 ± 5 nm in diameter	16 ± 1 nm in diameter	6 ± 0.8 nm in diameter	3 ± 1 nm in diameter	70 ± 5 nm in diameter	ligands in the range of 10~60 nm	3 nm in diameter (several hundred nm long)
Values of most negative electrode potential (ϵ_n/ mV)	411	410	404	376	378	359	252
Difference of electrode potential between samples[a] ($\Delta\epsilon_n$/ mV)	0	-1	-7	-35	-33	-52	-159
Difference of electrode potential between samples and $E_{PdCl_4^{2-}/Pd}$ ($\Delta\epsilon_n$/ mV)[b]	30	29	23	-5	-3	-22	-129

[a] The value of the most negative electrode potentials of Au^{QS}_{50} particles was set as the reference. [b] The $E_{PdCl_4^{2-}/Pd}$ is 381 mV vs Ag/AgCl.

Table S5. Summarized data of Pd contents, peak positions of $E_{Au\text{-}OH}$, $E_{Au\text{-}O}$, and $E_{Pd\text{-}O}$ of the resulting Au and Au@Pd NPs, and the electrode potential values of the corresponding nanoscale Au particles.

Samples	Au_{16}^{QS}	Au_{16}^{QS} + $PdCl_4^{2-}$	Au_{70}^{TOH}@Pd	Au_{3}^{QS}@Pd	Au_{10-60}^{AG}@Pd	Au_{3}^{NW}@Pd
Pd content/ %	0	0	0.89	1.56	2.5	8.0
E_{Au} / V	0.410	0.410	0.378	0.376	0.359	0.252
$E_{Au\text{-}OH}$ / $E_{Au\text{-}O}$ / V	-0.136/0.1	-0.136/0.1	～ / 0.1	～ / 0.1	～ / 0.1	～ / 0.1
$E_{Pd\text{-}O}$ / V	～[a]	～[a]	-0.145	-0.153	-0.162	-0.185

[a] The symbol "～"denoting the absence of corresponding peaks.

Table S6. Summarized values of the $f_{AGR}^{Au/Pd}$, the electrode potential of metal NPs (ϵ_{NP}) of Au_{50}^{QS}, Au_{16}^{QS}, Au_{6}^{QS}, Au_{3}^{QS} particle, Au_{70}^{TOH} particles, Au_{10-60}^{AG} and Au_{3}^{NW}.

Samples	$f_{AGR}^{Au/Pd}$	ϵ_{NP}/ mV
Au_{50}^{QS}	0	411
Au_{16}^{QS}	0	410
Au_{6}^{QS}	0	404
Au_{3}^{QS}	0.47	376
Au_{70}^{TOH}	0.42	378
Au_{10-60}^{AG}	0.51	359
Au_{3}^{NW}	0.76	252

Table S7. Summarized technique used for bulk percentage and surface coverage.

Composition of Au-Pd NPs	Technique
Bulk (%)	HAADF-STEM-EDS
Surface (%)	CVs obtained in 0.30 M N_2-saturated KOH solution

Table S8. Top view of models, work functions (ϕ, eV), variations in the work function (Δϕ, eV) and the formation energies of artifacial defects ($E_{formation}$, eV) of Au{111}, Au{100} and Au{110} facets with different ratios of artifacial surface defects (V_x^S) or artifacial subsurface defects (V_x^{SS}).

Orientation	Denotation	Top view of models	ϕ (eV)	Δϕ (eV)	$E_{formation}$ (eV)
Au{111}	$V_{3.13}^{S}$	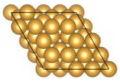	5.26	-0.07	0.99
	$V_{6.25}^{S}$	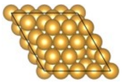	5.21	-0.12	1.88
	$V_{9.38}^{S}$	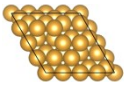	5.17	-0.16	2.87
	$V_{3.13}^{SS}$	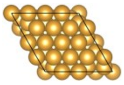	5.26	-0.07	0.02
	$V_{6.25}^{SS}$	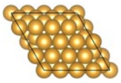	5.23	-0.10	0.35
	$V_{9.38}^{SS}$	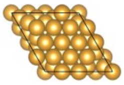	5.20	-0ϕ.13	0.64
Au{100}	$V_{3.13}^{S}$	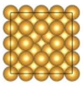	5.03	-0.02	0.58
	$V_{6.25}^{S}$	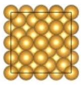	5.03	-0.02	1.05
	$V_{9.38}^{S}$	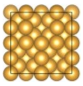	5.03	-0.02	1.07
	$V_{3.13}^{SS}$	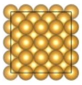	5.06	0.01	-0.19
	$V_{6.25}^{SSf}$	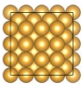	5.10	0.05	0.19
	$V_{9.38}^{SS}$	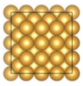	5.13	0.08	0.64
Au{110}	$V_{3.13}^{S}$	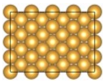	4.92	0.01	0.28
	$V_{6.25}^{S}$	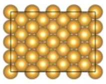	4.93	0.02	0.46
	$V_{9.38}^{S}$	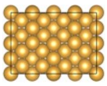	4.95	0.04	0.77
	$V_{3.13}^{SS}$	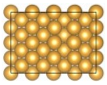	4.94	0.03	0.09
	$V_{6.25}^{SS}$	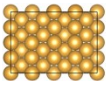	4.96	0.05	0.73
	$V_{9.38}^{SS}$	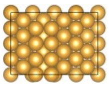	5.05	0.14	1.18

Computational Details. The density functional theory (DFT) calculations were implemented in the Vienna ab initio simulation package (VASP)[13, 14] using the Perdew−Burke−Ernzerhof (PBE) exchange-correlation functional of the generalized gradient approximation (GGA).[15, 16] The energy cutoff was set to be 450 eV, and the Brillouin zone sampling was performed using a 3 × 3 × 1 G-centered k-points. To model both the clean and defected Au{111}, Au{100} and Au{110} facets, a supercell containing five atomic layers of a 4 × 4 unit cell and a 20 Å vacuum region was used. During the geometry optimization of slabs with surface defects and subsurface defects, two and three topmost metal layers were allowed to relax, respectively.

The surface and subsurface of supercell contain 32 Au atoms. Removing one Au atom in the surface layer or subsurface layer in the supercell corresponds to defect ratios of 3.13%. Accordingly, defect ratios would increase to 6.25% and 9.38% by removing two and three Au atoms, respectively. As shown in Table S8, three different surface defects are formed by removing one center Au atom ($V_{3.13}^{S}$), two non-adjacent ($V_{6.25}^{S}$), and three non-adjacent ($V_{9.38}^{S}$) Au atoms of the surface layer. Moreover, three different subsurface defects are also formed by removing one center ($V_{3.13}^{SS}$), two non-adjacent ($V_{6.25}^{SS}$) and three non-adjacent ($V_{9.38}^{SS}$) Au atoms at the subsurface layer.

The stability of defected structures was examined according to the defect formation energy ($E_{formation}$), which was calculated as $E_{formation} = E_{defect} - E_{clean} + nE_{Au}$. E_{defect} and E_{clean} represent the total energies of the defected and clean surface structures, respectively. E_{Au} is the energy of per atom in the bulk Au, and n indicates the corresponding number of Au atoms removing from the clean Au{111}, Au{100} and Au(110) facets. Furthermore, the work function[17] (Φ), defined as the minimum energy to remove an electron from the facets, was calculated using the equation $\Phi = E_{vac} - E_F$, where E_{vac} and E_F correspond to energies the vacuum level and the Fermi level, respectively. The calculated work functions (Φ) of clean Au{111}, Au{100} and Au{110} facets are summarized in Table S9. The results are in excellent agreement with the theoretical work and experiments,[18, 19] showing that our methods and models are reliable.

As can be seen from Table S8, the formation energies of subsurface defects on Au{111} facet are lower than those of surface defects on Au{111} facet with the same defect ratio. Thus, subsurface defects are easier formed on Au{111} facet. So does Au{100} facet. As for the case of Au{110} facet, the formation energy of Au{110} with subsurface defects of 3.13% ($V_{3.13}^{SS}$) is much lower than that of Au{110} with surface defects of 3.13% ($V_{3.13}^{S}$). However, the formation energies of Au{110} with subsurface defects of 6.25% and 9.38% ($V_{6.25}^{SS}$ and $V_{9.38}^{SS}$) are much higher than those of Au{110} with surface defects of 6.25% and 9.38% ($V_{6.25}^{S}$ and $V_{9.38}^{S}$), respectively. Thus, Au{110} with surface defects are more stable when the defects of 6.25% and 9.38%.

Table S9. Summarized date for the calculated work functions (ϕ, eV) of clean Au{111}, Au{100} and Au{110} facets in this work and those reported in literature (including theoretical[18] and experimental values[19]).

Facets	ϕ (eV)		
	In this work	theoretical values[18]	Experimental values[19]
Au{111}	5.33	5.110	5.26 ± 0.04
Au{100}	5.05	5.071	5.22 ± 0.04
Au{110}	4.91	4.91	5.20 ± 0.04

Table S10. Comparison of the Plieth equation and our proposed general equation in this work.

Differences	Plieth equation	Equation in this work
Mathematical model	$\epsilon_{NP} = \epsilon_b + \epsilon_d = \epsilon_b - \frac{4\gamma v_m}{ZFd}$	$\epsilon_{AGR}^{Au/M} = \epsilon_b^{Au} + \sum_{\{hkl\}} \delta_{\{hkl\}}^{Au/M} \cdot R_{\{hkl\}}^{Au}$
Influence factors of electrode potential	NP size	surface topography
Applicable NP size	diameter (d) less than 6 nm	nanoscale

Table S11. Comparison of the ORR activity of different samples in 0.1 M KOH solution.

Samples	E_P (V)[a]	E_{onset} (V)[b]	$E_{1/2}$ (V)[b]	j (mA cm^{-2}) at 0.45 V[b]	Tafel slope (mV dec^{-1})
Au_3^{QS}/C	0.78	0.951	0.80	2.85	60.1
Au_{70}^{TOH}/C	0.74	0.949	0.79	2.98	69.3
Au_{10-60}^{AG}/C	0.79	0.955	0.81	3.4	59.7
Au_3^{NW}/C	0.805	0.971	0.822	3.61	53.6

[a] Ep were determined from cyclic voltammograms (Fig. 5A). [b] $E_{1/2}$ and j at 0.45 V were determined from rotating disk voltammograms with a rotation speed of 1600 rpm (Fig. S14).

References

(1) H. Xia, Y. Xiahou, P. Zhang, W. Ding, and D. Wang, *Langmuir* 2016, **32**, 5870–5880.

(2) W. Duan, P. Zhang, Y. Xiahou, Y. Song, C. Bi, J. Zhan, W. Du, L. Huang, H. Möhwald, and H. Xia, *ACS Appl. Mater. Interfaces* 2018, **10**, 23081–23093.

(3) S. Biggs, P. Mulvaney, C. F. Zukoski, and F. Grieser, *J. Am. Chem. Soc.* 1994, **116**, 9150–9157.

(4) J. G. Smith, and P. K. Jain, *J. Am. Chem. Soc.* 2016, **138**, 6765–6773.

(5) J. Li, R. R. Nasaruddin, Y. Feng, J. Yang, N. Yan, and J. Xie, *Chem. Eur. J.* 2016, **22**, 14816–14820.

(6) R. Dinkel, J. Jakobi, A. R. Ziefuß, S. Barcikowski, B. Braunschweig, and W. Peukert, *J. Phys. Chem. C* 2018, **122**, 27383–27391.

(7) R. A. Masitas, and F. P. Zamborini, *J. Am. Chem. Soc.* 2012, **134**, 5014–5017.

(8) A. Al-Akl, and G. A. Attard, *J. Phys. Chem. B* 1997, **101**, 4597–4606.

(9) S. L. Allen, J. N. Sharma, and F. P. Zamborini, *J. Am. Chem. Soc.* 2017, **139**, 12895-12898.

(10) X. Huang, A. J. Shumski, X. Zhang, and C. W. Li, *J. Am. Chem. Soc.* 2018, **140**, 8918–8923.

(11) Y. Song, T. Miao, P. Zhang, C. Bi, H. Xia, D. Wang, and X. Tao, *Nanoscale* 2015, **7**, 8405–8415.

(12) J. Wang, J. Gong, Y. Xiong, J. Yang, Y. Gao, Y. Liu, X. Lu, and Z. Tang, *Chem. Commun.* 2011, **47**, 6894–6896.

(13) G. Kresse, and J. Hafner, *Phys. Rev. B* 1993, **47**, 558-561.

(14) G. Kresse, and J. Furthmüller, *Phys. Rev. B* 1996, **54**, 11169-11186.

(15) J. P. Perdew, K. Burke, and M. Ernzerhof, *Phys. Rev. Lett*. 1996, **77**, 3865-3868.

(16) P. E. Blöchl, *Phys. Rev. B* 1994, **50**, 17953-17979.

(17) P. C. Rusu, and G. Brocks, *J. Phys. Chem. B* 2006, **110**, 22628-22634.

(18) J. Wang, and S.-Q. Wang, *Surf. Sci.* 2014, **630**, 216-224.

(19) G. V. Hansson, and S. A. Flodström, *Phys. Rev. B* 1978, **18**, 1572-1585.